Journal of Petroleum Science and Engineering 187 (2020) 106746

Contents lists available at ScienceDirect

Journal of Petroleum Science and Engineering

journal homepage: http://www.elsevier.com/locate/petrol

Comparing mechanical and ultrasonic behaviour of a brittle and a ductile shale: Relevance to prediction of borehole stability and verification of shale barriers

Rune M. Holt [a,*], Idar Larsen [b], Erling Fjær [c], Jørn F. Stenebråten [b]

[a] NTNU (Norwegian University of Science and Technology), Geoscience and Petroleum Department, Trondheim, Norway
[b] SINTEF Industry, Trondheim, Norway
[c] SINTEF Industry & NTNU (Norwegian University of Science and Technology), Trondheim, Norway

ARTICLE INFO

Keywords:
Shale
Borehole stability
Shale barrier
Acoustic logging

ABSTRACT

Borehole collapse during drilling operations in shale formations is a well-known and costly problem within the petroleum industry. Recently it has become evident that shales may also form sealing barriers around the casing, reducing the need for cement jobs on new wells, and reducing costs for plugging and abandonment of old wells. The forming of such barriers involves large deformations of shale through creep and plastic processes. Hence, it is important to be able to characterize to what extent shales may fail in a brittle or ductile manner, in both cases causing possible hole instabilities during drilling, and in the case of ductile shales, enabling permanent sealing barriers. Triaxial failure tests, creep tests and tests tailored to follow the failure envelope under simulated borehole conditions have been performed with two soft shales. One shale fails in a more brittle manner than the other and fails to form a sealing barrier in the laboratory. The more ductile shale has been proved to form barriers both in the laboratory and in the field. By comparing their behavior, it is seen that the ductile shale exhibits normally consolidated behaviour, while the more brittle shale is overconsolidated. This points to the stress history and possibly cementation as keys in determining the failure mode. In addition, porosity, clay content, ultrasonic velocities, unconfined strength and friction angle may be used as indicators of brittle or ductile post-failure behaviour. Ultrasonic velocity and in particular attenuation measurements are shown to be sensitive to the failure initiation process, although stress sensitivity is much lower in the ductile than in the brittle case. The experiments provide values for anisotropic velocities as well as P-wave impedances that are necessary for open as well as cased hole log interpretation, in particular for barrier verification and possibly for monitoring of barrier formation.

1. Introduction

Borehole failure in shale formations is a key to tight hole/stuck pipe situations during drilling (e.g. Fjær et al., 2008; Ch.9). Drillers often distinguish between "sloughing" shale and "gumbo" shale. The former translates in rock mechanics language to brittle failure, resulting in formation of breakouts and rock fragments falling into the hole, hampering the motion of the drill string. "Gumbo" shale, on the other hand, describes a ductile failure mode, where large (plastic) deformation leads to borehole closure around the drill string. Over the last decades, the petroleum industry has strived to predict and mitigate such failures during drilling operations, using tailored mud weight and mud composition in terms of oil vs water-based systems, salinity, type of salt, and other additives. All shales exhibit some degree of plasticity, and it is well established (e.g. Holt et al., 2015) that this plays an important role in predicting accurate values for the critical mud weight leading to hole collapse: Plasticity is good for borehole stability, but so is high strength – and the two do not normally correlate.

Contrary to borehole collapse during drilling, shale failure has however also proved to be useful: Successful natural shale barriers have been reported, where the annulus between casing and formation has closed after drilling, forming an efficient seal (Williams et al., 2009; Kristiansen et al., 2018). This is of large importance for plug and abandonment of oil wells but may also be considered as an alternative to

* Corresponding author.
E-mail addresses: rune.holt@ntnu.no (R.M. Holt), idar.larsen@sintef.no (I. Larsen), erling.fjaer@sintef.no (E. Fjær), Jorn.Stenebraten@sintef.no (J.F. Stenebråten).

https://doi.org/10.1016/j.petrol.2019.106746
Received 27 June 2019; Received in revised form 24 November 2019; Accepted 26 November 2019
Available online 30 November 2019
0920-4105/© 2019 The Authors. Published by Elsevier B.V. This is an open access article under the CC BY license (http://creativecommons.org/licenses/by/4.0/).

cement in new wells, provided that the barrier has sufficient thickness and is formed fast enough. Obviously, the well needs to be completed in a stable condition prior to the formation of the barrier. Intuitively, to obtain as good seal as possible, the ductile mode of failure is in this case preferable compared to the brittle mode.

Initiation of borehole instabilities as well as formation of shale barriers are driven by stresses close to a fluid filled opening, either a borehole or an annulus outside a casing. In the case of a barrier, stresses will change when the barrier forms and pressure on the casing builds up. For extremely soft shales, the annulus may close while the rock is still in a state of strain hardening. For most shales, the annulus may close only if the rock nearest to the borehole wall is brought beyond peak stress. This post peak material may form a sealing barrier against the casing if it deforms in a ductile manner. On the other hand, if it deforms in a brittle manner, the annulus will most likely be filled with a heavily fractured and highly permeable material with poor sealing ability. In both cases, the rock will be in contact with the casing and thus bring about a response on cased hole logging tools. It is therefore important to identify detectable features that can be used to distinguish between the two cases, both in the planning phase prior to completion, and in the verification phase during interpretation of the cased hole logs. Note that the barrier forming process develops in a combination of consolidation and creep and may also occur prior to a cementing operation, in which case this operation will be hampered.

Theoretically, the stress state around boreholes is well understood and described, incorporating plasticity as well as chemical and thermal effects (Fjær et al., 2008). Experimentally, borehole failure (e.g. Guenot, 1989; Marsden et al., 1996; Gabrielsen et al., 2010; Meier et al., 2013) can be simulated in down-scaled hollow cylinder tests. A tailor-made shale barrier test (Fjær et al., 2018) has been developed, using a metallic tube to represent the casing. A pre-drilled hole is made with larger diameter than the tube, to establish an initial annulus, similar to a field situation. Hole failure is initiated by application of an external stress being sufficiently larger than the fluid pressure in the annulus. This may or may not result in a sealing barrier. Fig. 1 shows μCT scans of two shale samples after such a test, illustrating brittle (left) and ductile (right) failure modes.

Tests like those described above are valuable in order to compare with field experience and to gather data for prediction of future field operations. They also give insight into physical mechanisms. If core plugs are available for standard triaxial, while the more sophisticated hollow cylinder tests or shale barrier tests can not be performed (these tests usually require larger samples than standard core plug tests), supplementary information from controlled experiments may add valuable understanding of the failure process and establish input data for assessment or borehole stability or potential for formation of a natural barrier. In addition, studies of P- and S-wave propagation during such tests provide information of relevance for interpretation of sonic open hole and sonic/ultrasonic cement bond logging (Holt et al., 2017). Sonic log data can be used in the drilling phase as input to borehole stability analysis by estimating shale strength through empirical correlations (e.g. Horsrud, 2001), and further has a potential for selection of formations that are likely to form barriers around the casing. Cased hole logging (Allouche et al., 2006; De Bruin et al., 2016) is required, along with pressure testing, for verification of barriers in the well completion or in the well plugging phase. For plug and abandonment (P & A) of old wells, cased hole logging also provides valuable information on the state of cement or natural barriers behind the casing.

Conventional cement bond logging has been applied in shale barrier verification (e.g. Williams et al., 2009; Kristiansen et al., 2018). Traditionally, a sonic technique (CBL) has been used in cased boreholes, but this does not permit characterization of the material outside the casing, except for characterizing the presence and to some extent the quality of the bond between the casing and the surrounding material (cement/-formation). Today, the pulse-echo technique (e.g. Havira, 1982; Hayman et al., 1991) is commonly used, along with the pitch-catch technique (e.g. Van Kuijk et al., 2005). Both methods operate in the ultrasonic domain between 100 and 700 kHz. In the pulse-echo technique, an ultrasonic pulse is transmitted from the wellbore against the casing, and the reflected signal is detected. The ringdown (coda) of this signal is used to measure an attenuation coefficient, which can be related to reflection of the pulse due to acoustic impedance contrast between the casing steel and the medium outside. If there is a bond between cement/formation and casing, the attenuation increases with increasing acoustic impedance of the material behind the casing. With the pitch-catch technique, which can be used as a supplement to the pulse-echo method, the attenuation of a flexural wave travelling along the casing is measured and related to the P-wave velocity of the contacting medium (cement, shale, etc).

In this paper we will compare the two relatively soft and weak shales illustrated in Fig. 1. One of the aims is to identify mechanical behavior and characteristic parameters of the shale that control to what extent the failure mode of the borehole is brittle or ductile. Part of this is to identify typical ultrasonic impedance and velocity that one would expect to measure in a sonic log within the intact shales, and which would be representative for a shale barrier behind the casing. The experimental program and the experimental results, described in the next paragraphs, includes three different types of tests performed with both shales: (i)

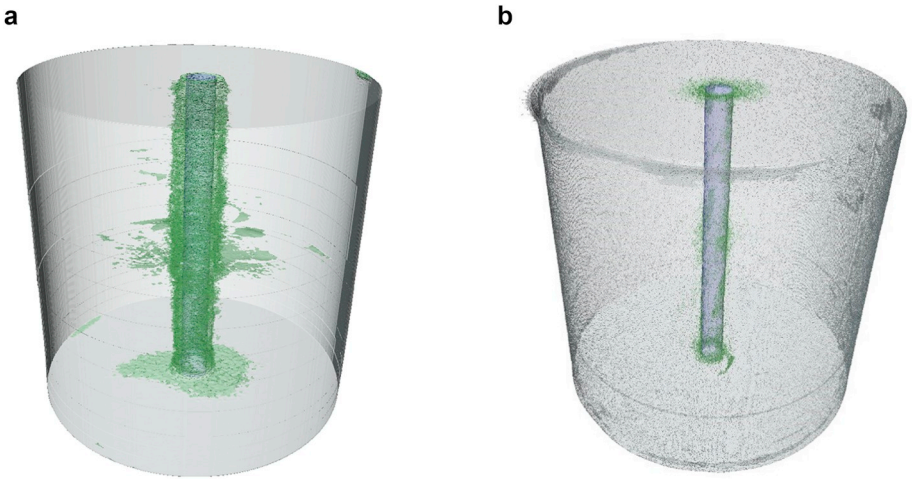

Fig. 1. Examples of μCT images after shale barrier tests with two different shales. The green colour represents void space. The image to the left reveals brittle failure (in Pierre Shale) with localized breakouts in the annulus, while the image to the right shows a shale (S Shale) where ductile failure has led to closure of the annulus. (For interpretation of the references to colour in this figure legend, the reader is referred to the Web version of this article.)

Consolidated Undrained (CU) triaxial tests, (ii) Constant mean stress undrained creep tests, and (iii) Specially designed tests where stresses are controlled to mimic changes around a borehole/annulus when the well pressure is reduced and the shale is permitted to fail. In all experiments the tests were monitored by ultrasonic wave propagation. In the paragraphs devoted to experimental results, the measured data are shown, with focus on comparison between the behaviours of the two shales. Field implications of the experimental observations for borehole failure and barrier formation are discussed. In addition to a microscopic interpretation of the ultrasonic data, the impact of the laboratory measurements on interpretation of open and cased hole sonic and ultrasonic log data is described. Along with evaluation of mechanical behaviour from sonic logs in neighbouring wells ahead of drilling and evaluation and possible monitoring of shale barrier formation from cased hole logging. Conclusions focus on possible attributes of brittle vs ductile behavior that can be taken from laboratory or field log data, and in particular on learnings from the ultrasonic measurements presented in this paper.

2. Shales and shale characterization

The experimental study was done with an outcrop (Pierre I Shale) and a field shale (named S Shale), with porosity, mineralogy and key rock mechanical properties as given in Table 1. The S Shale has been proven to form a sealing barrier in situ as well as in the laboratory (Fig. 1, right), while Pierre I Shale (Fig. 1, left) did not form a barrier when studied in the laboratory. As an outcrop, it is not relevant to address its behavior in a field situation, but mechanically Pierre I Shale resembles several overburden shales of interest to the petroleum industry.

Both shales have been stored in oil until the time of testing to be protected from dehydration, and core plugs were also drilled using oil as circulating and cooling fluid. All cores were exposed to 3.5% NaCl brine during the laboratory experiments, after they had been placed under a nominal confining pressure. Subsequent application of stress and pore pressure enables full saturation to be reached without damaging the samples (Horsrud et al., 1998). Measurement of the pore pressure response verifies that saturation is achieved. Porosity was determined by water loss in a piece of the core after heating to 110 °C for sufficiently long time to equilibrate its weight. Sample volume was measured by its buoyancy. Water content was derived from the same measurement as the ratio between the weight of displaced water and the sample. Mercury injection porosimetry shows lower porosities than the water content data, because the narrowest pores are not captured by this technique. Predominant pore sizes are typically 20–30 nm in both shales, but Pierre shows an additional broad tail of larger pores (0.1–10 μm). Clay content was determined with X-Ray Diffraction (XRD), grouping all clay minerals together, Analysis of fine fractions (<2 μm diameter particles) reveals the presence of smectite in both shales, particularly in S Shale. The specific surface area was measured by nitrogen adsorption (BET technique). Strength parameters (unconfined strength and friction) angle were derived from undrained triaxial tests, described in the next paragraph. The unconfined strength and friction angle as listed in Table 1 were obtained with maximum principal stress along the symmetry axis. The shales do exhibit anisotropy, which will be considered below when ultrasonic wave propagation is addressed.

Table 1
Petrophysical and rock mechanical key parameters of Pierre I Shale and S Shale.

	Pierre I Shale	S Shale
Density [g/cm^3]	2.39	2.16
Porosity [%]	21	39
Water content [%]	9	18
Clay content [%]	48	62
Quartz content [%]	27	15
Specific surface [m^2/g]	17	40
Unconfined Strength [MPa]	9.7	6.2
Friction angle [°]	30	13

3. Rock mechanical characterization

3.1. Test procedures for consolidated undrained (CU) triaxial tests

Consolidated undrained (CU) triaxial tests were performed with brine-saturated samples of Pierre I Shale and S Shale. The purpose of such tests is to obtain strength parameters (unconfined strength UCS and friction angle), which are necessary for borehole stability analysis and hence also for shale barrier evaluation. In both cases, distinguishing between brittle and ductile/plastic behavior is important. This calls for measurable attributes. The tests were done with three plugs from each shale at three different confining pressures. Pierre I Shale samples were small, in order to limit the duration of the tests: Diameter was 15 mm and sample length around 30 mm. S Shale samples were tested in a different triaxial cell, with 76 mm sample length and 38 mm diameter. The difference in sample size was due to different practical purposes of the tests, but given the small grain sizes of shales, they are both within ISRM standards considering samples that are not intersected by fractures on a larger length scale (Nes et al., 2004). All tests were performed at room temperature, with the sample axis normal to the bedding plane. Ultrasonic P-wave velocities were measured by pulse transmission along the sample axis in all tests. In S Shale, P-wave measurements were also performed normal to the sample axis. The frequency was 0.5 MHz.

The samples were initially loaded in drained conditions to an isotropic stress (confining pressure = axial stress) with a controlled pore pressure. This initial pore pressure was 5 MPa for Pierre I Shale and 17 MPa (close to the in-situ value) for S Shale, while the confining pressures were 5–20 MPa higher than the pore pressures. The effective stress controlling failure is generally agreed to be the net stress = confining pressure minus pore pressure. Initial net stresses were 5, 10 and 15 MPa for Pierre I Shale and 5, 10 and 20 MPa for S Shale. After equilibration in each test, the axial stress was increased in undrained conditions, keeping constant confining pressure, measuring the pore pressure response. The net axial stress (peak stress minus accompanying pore pressure) and the net confining pressure at failure were used to derive the strength parameters (unconfined strength and friction angle in Table 1) by fitting the data to a linear Mohr-Coulomb criterion.

3.2. Experimental results from CU triaxial tests

The CU triaxial test results are summarized in a so-called q,p' plot (Fig. 2), adapted from soil mechanics (e.g. Atkinson and Bransby, 1978). This plot shows the evolution of shear stress (q on the vertical axis denotes axial minus radial stress, which is twice the maximum shear stress in the sample) during the triaxial tests against net mean stress (denoted p'), which is the mean stress minus the pore pressure. The net stress is considered the effective stress controlling rock failure process, and differs from the effective stress controlling deformation: In that case, the pore pressure is weighted with a poroelastic (Biot) coefficient ≤ 1. The peak stress of each curve represents the strength at each level of confining pressure and forms the basis for estimation of unconfined strength and friction angle as given in Table 1. The plot shows that Pierre I Shale is stronger than S Shale at all stress levels, and that its strength increases more rapidly with increasing confining pressure, reflecting the higher value of the friction angle. Furthermore, S Shale shows characteristic behaviour of a normally consolidated material (in geotechnical terminology: a material that is brought beyond the maximum stress experienced previously). This is seen by the tendency of the q vs p' curves to lean towards the left during the failure process, reflecting that the pore pressure increase exceeds the increase in mean stress. Pierre I Shale, however, exhibits behavior characteristic of overconsolidated or cemented rock. Pierre I Shale samples dilate during failure at all confining pressures, while all S Shale samples contract. Notice that both

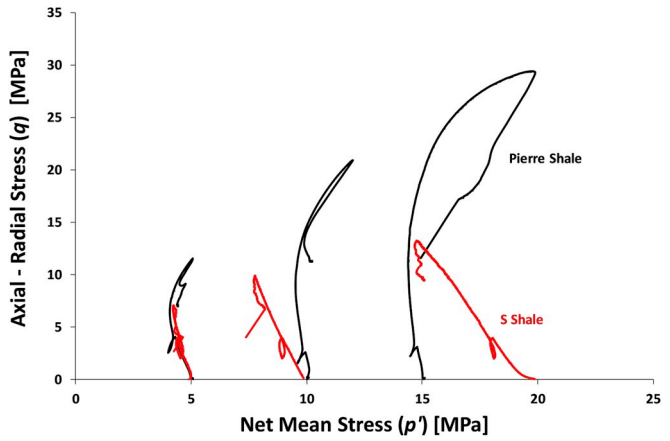

Fig. 2. *q-p*'plot, i.e. q = σz- σr vs net mean stress p'= (σz+2 σr)/3-*p*f from consolidated undrained triaxial tests with Pierre I Shale (black curves) and S Shale (red curves) at different confining pressures. Axial stress was applied along the symmetry axis (normal to bedding) in both shales. (For interpretation of the references to colour in this figure legend, the reader is referred to the Web version of this article.)

shales soften after peak stress, in particular at low confining pressures. Adding more laboratory data confirms that normal consolidation behavior appears characteristic for barrier forming shales. (Holt et al., 2019).

Ultrasonic P-wave velocities are shown vs. axial strain in Fig. 3, and key values are listed in Table 2. The velocities are higher in Pierre I Shale than in S Shale. In both shales, velocities increase with increasing confining pressure, also more in Pierre Shale. During each test, axial P-wave velocities (v_{Pz}) increase with axial strain (and axial stress) as the samples approach failure. The strain (and stress) sensitivity is higher in Pierre I Shale than in S Shale at all confining pressures. The R factor given in the table is the strain sensitivity, defined as (Hatchell and Bourne, 2005; Røste et al., 2006):

$$R = \frac{\Delta v_{Pz}}{v_{Pz}} \cdot \frac{1}{\Delta \varepsilon_z}. \quad (1)$$

Axial strain is denoted by ε_z, and the tabulated R is the axial P-wave

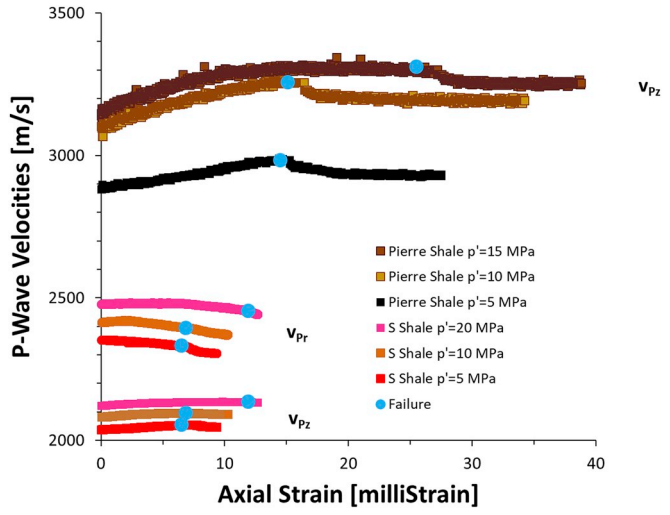

Fig. 3. P-wave velocities normal to bedding (v_{Pz}) for Pierre I Shale and S Shale, and Pwave velocity parallel to bedding (vPr) for S Shale, plotted against axial strain for CU triaxial tests starting from different initial net confining pressures (p'). The strain levels where peak stress was reached in the individual tests are marked with blue dots. (For interpretation of the references to colour in this figure legend, the reader is referred to the Web version of this article.)

velocity change Δv_{Pz} accompanying a strain $\Delta \varepsilon_z$ occurring from start of axial loading until peak stress in the triaxial segments of the tests (listed in the caption of Fig. 3) ($v_{Pz}$is the initial velocity). Note that strain is positive for compaction, so a positive value for R indicates velocity increase with increasing stress that leads to axial compaction. The R value for Pierre I Shale is larger than that for S Shale. The strain sensitivity decreases with increasing confining pressure, partly because the samples strain more before they fail. The radial P-wave velocity (v_{Pr}) that was measured for S Shale is also shown in Fig. 3 and given in Table 2. The radial velocities are larger than the axial velocities, reflecting lithological anisotropy. The P-wave anisotropy, at any stress level, expressed as Thomsen's anisotropy parameter

$$\varepsilon_{Th} = \frac{v_{Pr}^2 - v_{Pz}^2}{2v_{Pz}^2} \quad (2)$$

is ~0.17 at the start of the triaxial segments. When the sample starts to yield, the radial velocities start to decrease at all confining pressure, leading to a reduced anisotropy (~0.15) at the peak stress. The R factor is also defined with respect to axial strain for the radial velocity change, and as shown in Table 2, it becomes negative. After failure, all velocities are seen to drop slightly, apparently reaching a more or less constant level.

4. Undrained creep tests

4.1. Test procedures

Consolidated undrained creep tests have been performed with brine-saturated core plugs of Pierre I Shale and S Shale. The main purpose of these tests was to see if approaching failure by time dependent deformation (creep) would lead to differences in strain response, strain dependence of ultrasonic velocities, and failure mode, when compared with the standard CU tests presented above. These are not standard tests in rock mechanical core testing, but they are relevant when time dependent failure processes are analyzed. The test was performed in constant mean stress conditions, which is valid for the stress state far from the borehole wall, where the rock is in an elastic state until it reaches failure. A motivation was thus to see if failure initiation was comparable in terms of peak stress and brittle or ductile behavior compared to the CU triaxial tests.

The core plugs were cylinders with diameter 25.5 mm and ~50 mm length, both drilled with the sample axis normal to the bedding plane. The samples were placed in an triaxial system, where axial and radial stresses were controlled and measured, while axial strain was measured as the average of three LVDT recordings and radial strains were obtained in two orthogonal directions with strain gages mounted to a cantilever system. Axial ultrasonic velocities were measured throughout the tests with the pulse transmission technique, using broadband P-wave transducers with 1 MHz center frequency. The samples were first loaded to 15 MPa isotropic stress and 7 MPa pore pressure, and then heated to 40 °C. This initiation phase lasted approximatively 50 hours. The samples were then exposed to stepwise undrained axial loading and radial unloading under constant mean stress conditions (see Figs. 4, 5), maintaining constant temperature. The pore pressure response was measured using a small dead volume less than 10% of the pore volume. The axial stress increase was 1.5 MPa (hence the corresponding radial stress decrease was 0.75 MPa) in each step. Notice that we use the terms radial stress and confining pressure synonymously. The external stresses were increased relatively fast (typically within ~5 min), while they were held at the target stress level of each step for 8–16 hours. This is sufficient for pore pressure and hence strains as well as ultrasonic velocities to equilibrate, except in the last steps, where the samples creep towards failure.

Table 2
Axial P-wave velocities at the initial state and at the failure state for Pierre I Shale and S Shale. Radial P-wave velocities were also measured for S Shale. The strain sensitivity factors R_{Pz} and R_{Pr} (eq. (1)) are also listed. The Pierre Shale samples were too small to permit radial P-wave velocity measurement, but v_{Pr} was measured in the borehole stress path tests (Table 4).

Pierre I Shale	Initial stresses [MPa]	v_{Pz} [m/s]	v_{Pr} [m/s]	Failure state [MPa]	v_{Pz} [m/s]	v_{Pr} [m/s]	R_{Pz}	R_{Pr}
	$p' = 5$, $q = 0$	2881		$p' = 5.0$, $q = 11.4$	2987		2.5	
	$p' = 10$, $q = 0$	3102		$p' = 12.0$, $q = 20.8$	3256		3.3	
	$p' = 15$, $q = 0$	3140		$p' = 19.9$, $q = 29.4$	3301		2.1	
S Shale	$p' = 5$, $q = 0$	2038	2352	$p' = 4.3$, $q = 6.7$	2054	2327	1.2	−1.6
	$p' = 10$, $q = 0$	2082	2416	$p' = 7.8$, $q = 9.9$	2096	2396	1.0	−1.2
	$p' = 20$, $q = 0$	2122	2473	$p' = 14.8$, $q = 12.2$	2135	2450	0.5	−0.8

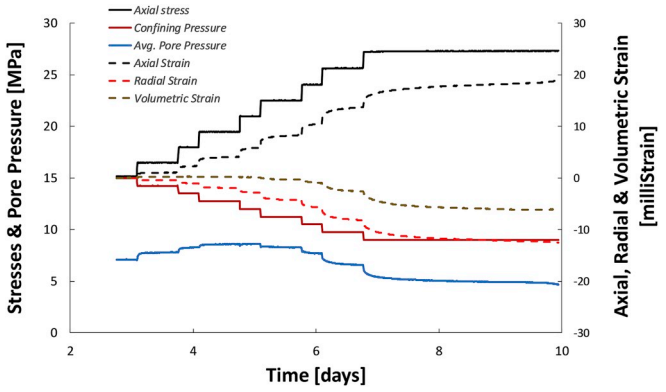

Fig. 4. Stresses, pore pressure and strains during the undrained constant mean stress test with Pierre I Shale.

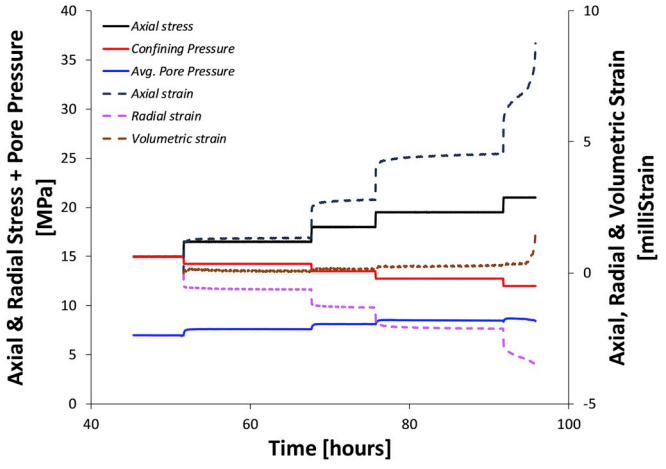

Fig. 5. Stresses, pore pressure and strains during the undrained constant mean stress test with S Shale.

4.2. Results from CU creep tests

Figs. 4, 5 show the strain and pore pressure evolution during the undrained constant mean stress tests with Pierre I Shale and S Shale. In both cases, failure occurred during the last step: For Pierre I Shale, a distinct shear band was formed, at the same time as the sample dilated and the pore pressure decreased. In S Shale, there is also evidence of shear failure, however, the shear band is more diffuse. This sample shows tertiary (accelerating) creep and maintained close to zero volumetric strain before it contracted slightly during failure. Pore pressure increased but appears to decrease slightly at the very end of the test. The q-p' plot in Fig. 6 shows that both samples initially exhibit normally consolidated behaviour. Pierre I Shale changes trend above q~9 MPa to behaviour which is characteristic of overconsolidation or cementation.

The behaviour of the two shales in the creep tests with constant mean stress segments fits well into to that seen from triaxial tests in Fig. 2, in spite of the different sample sizes used in the different experiments, and in spite of slight differences in stress conditions and temperature. Note that estimated static shear moduli at 50% of peak shear stress are ~0.6–0.7 GPa for both materials. For comparison, the corresponding shear moduli in the CU triaxial test at 10 MPa initial net mean stress are similar: ~0.5 GPa for S Shale and 0.6 GPa for Pierre Shale. Note that these moduli refer to initial loading.

Axial P-wave velocities for the two shales against axial strain (measured from the start of the first constant mean stress stage) are shown in Fig. 7, and listed for selected stress levels (including failure) in Table 3. Pierre I Shale again has higher P-wave velocity than S Shale (2740 m/s vs. 2050 m/s at the initial stress level). The overall picture is that both shales show increasing velocity with increasing compaction, and that the velocity change close to failure is very small. The same trend can also be seen during the individual load steps, where strains are caused partly by consolidation and partly by creep. The velocity increase from initial stress to failure is ~90 m/s for Pierre I Shale, while it is only ~15 m/s for S Shale. These numbers are in close agreement with the results of the triaxial tests (Fig. 3), again in spite of difference in the test procedures. Notice that the axial strain where failure takes place also is similar for all tests. The average value of the strain sensitivity parameter R is 2.2 for Pierre I Shale and 1.2 for S Shale, reduced to ~1 in the final load stage for Pierre I Shale and close to zero for S Shale. Although quite similar to the numbers in Table 2, the difference in stress path (constant mean stress vs triaxial) is expected to cause a slightly lower R-value (Holt et al., 2018). This is primarily because of expected higher axial strain for a constant mean stress path than for purely axial loading, but as pointed out above, strain differences are small in these tests.

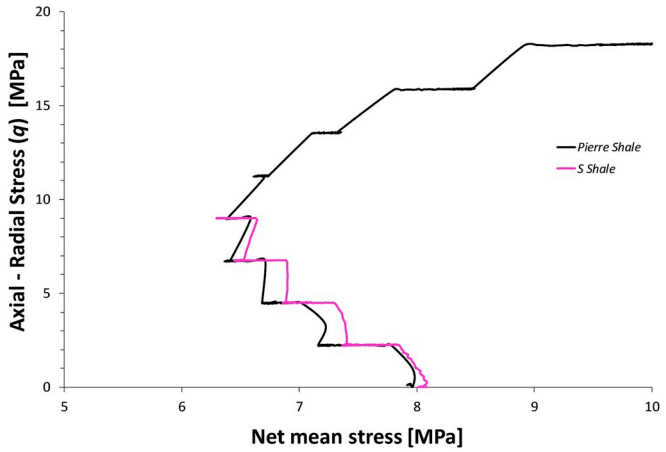

Fig. 6. q-p'plot, i.e. $q = \sigma z - \sigma r$ vs net mean stress $p' = (\sigma z + 2\,\sigma r)/3$-$pf$ from the undrained constant mean stress creep tests with Pierre I Shale (black curves) and S Shale (red curves) at different confining pressures. (For interpretation of the references to colour in this figure legend, the reader is referred to the Web version of this article.)

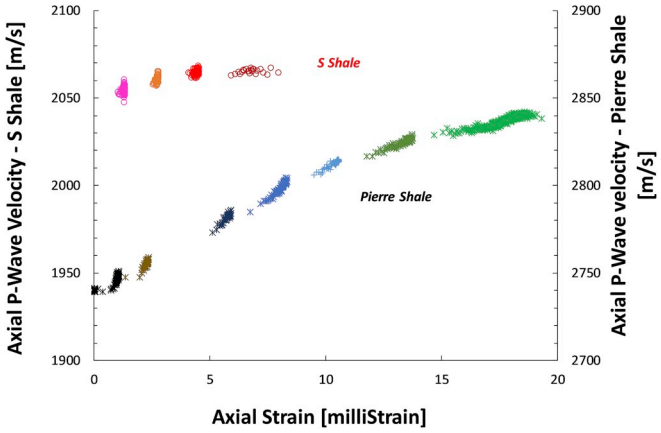

Fig. 7. Measured axial ultrasonic P-wave velocities during the creep stages of the undrained constant mean stress tests with S Shale (left vertical axis) and Pierre I Shale (right vertical axis).

Table 3
Axial P-wave velocities after the initial state and after selected creep stages (including the failure state) in the undrained constant mean stress tests with Pierre Shale and S Shale.

Pierre I Shale	Stress state [MPa]	v_{Pz} [m/s]	S Shale	Stress state [MPa]	v_{Pz} [m/s]
	$p' = 8.0$, $q = 0.2$	2740		$p' = 8.0$, $q = 0.0$	2051
	$p' = 6.4$, $q = 9.0$	2782		$p' = 6.9$, $q = 4.5$	2063
	$p' = 8.5$, $q = 15.9$	2827		$p' = 6.5$, $q = 6.8$	2065
	$p' = 10.4$, $q = 18.3$	2839 (failure)		$p' = 6.5$, $q = 9.0$	2065 (failure)

5. Borehole stress path tests

5.1. Test procedures

The core plug tests described below have been performed in a conventional triaxial cell with the aim of simulating stress changes in shale near a borehole wall (or outside the annulus surrounding a casing until and beyond failure initiation, and finally to follow the failure envelope. In this way, acoustic properties characteristic of a barrier forming material can be measured. This helps to distinguish between a shale barrier and fluids or cement behind the casing, and possibly also to assess the sealing quality of the barrier. In addition, this experiment also gives fundamental understanding and insight into the mechanical processes responsible for brittle and plastic failure and the associated changes in ultrasonic properties.

Since only the maximum and minimum principal stresses can be controlled, biaxial tests can not reproduce the full triaxial nature of the in situ stresses near a borehole. Stresses are thus tailored to mimic in situ conditions, moving from the initial pre-drilling stress state to the near borehole stress state during and after drilling. As known from rock mechanics literature (see Fjær et al., 2008, for a summary), shear failure, being responsible for hole collapse as well as formation of shale barriers, can be triggered by the tangential (hoop) stress (described as "case a") or by the axial stress ("case b") being the maximum principal stress near the borehole wall, while the radial stress (equal to the well or annulus pressure) is the minimum principal stress. In a core test, one can reinstall the in situ stress state prior to drilling the hole by applying the in situ vertical stress as axial stress along the core axis and an assumed isotropic horizontal stress as confining pressure. If the symmetry axis of the shale in situ is vertical and the core is oriented the same way, then only the case when failure is caused by axial stress being the maximum ("case b") can be mimicked in a conventional triaxial laboratory set-up (the case with the tangential stress being the maximum requires a true triaxial set-up) (illustrated in Fig. 8). In the present case the confining pressure initially represents the in situ horizontal stress, but as the borehole simulation test progresses, it is reduced, simulating the radial stress decrease around the borehole with decreasing well pressure, or with reduced distance to the borehole wall. When failure is initiated, and plastic deformation starts to dominate, both axial stress and confining pressure will have to be decreased, and they are here decreased at the same rate. The pore pressure is kept constant, mimicking an impermeable borehole wall situation. The idealized timeline corresponding to this experimental simulation is shown schematically in Fig. 8, along with the stress profile behind the wall of the borehole/annulus.

The experiments with Pierre I Shale and S Shale were performed in a different load frame with a different triaxial cell from that used for the undrained creep tests (see above). Samples were 38 mm (1 ½ ") in diameter and 75–80 mm long. Again, axial stress and confining pressure were controlled, and in addition the pore pressure was kept constant (at 5 MPa) throughout the tests. Axial strain was determined on the basis of 2 LVDTs, while radial strain was measured using an MTS circumferential extensometer. Ultrasonic P-wave velocities were measured by pulse

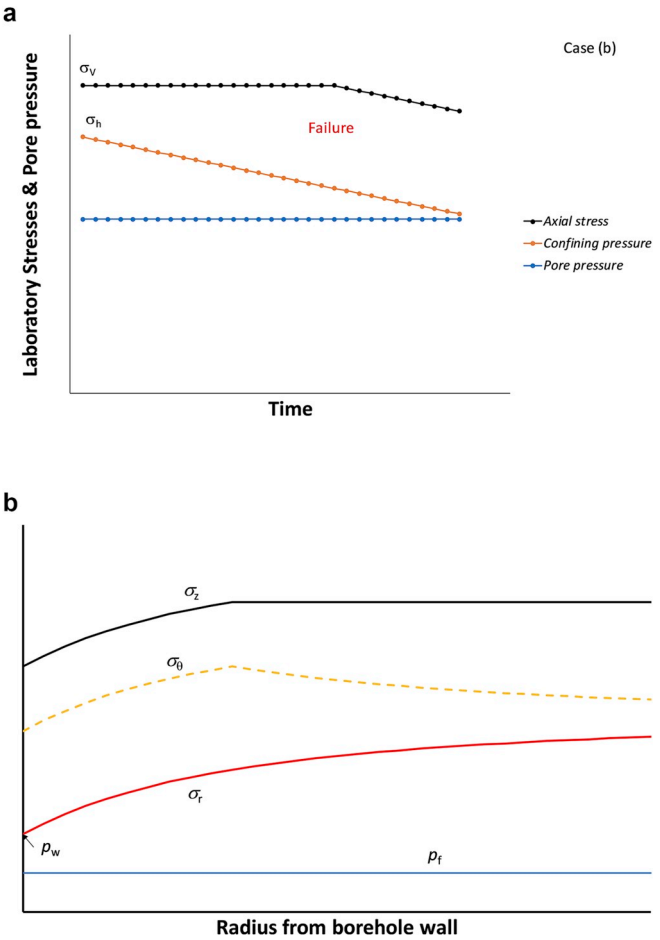

Fig. 8. The upper part shows schematic stress changes with shale cores in order to mimick the change in borehole (or annulus) stresses during reduction of well (or annulus) pressure. The initial axial and confining stresses correspond to in situ vertical and horizontal stress, respectively, while they represent the axial and radial stresses at the borehole wall during the test itself. When failure is initiated, the axial and radial stress decrease at the same rate, imitating an ideal plastic stress distribution around the borehole, as shown in the lower part of the figure. The figure is based upon Tresca's failure criterion, i.e. Mohr-Coulomb with zero friction angle.

transmission along the sample axis and in two orthogonal directions normal to the sample axis. Broadband transducers with 500 kHz central frequency were used. Attenuation (α) was estimated individually for each test using the spectral ratio method

$$\alpha(f,n) = \frac{20\log_{10}\left[FFT(WF_{ref})/FFT(WF_n)\right]}{L_{sample}} \quad (3)$$

where $FFT(WF_{ref})$ is the frequency spectrum of an arrival in the reference waveform, $FFT(WF_n)$ is the frequency spectrum of the arrival in waveform n and L_{sample} is the length of the sample. The reference waveform was chosen as the waveform with highest energy in the test.

Pierre I Shale was loaded in two steps to reach the initial stress state (20 MPa axial stress, 13 MPa confining pressure and 5 MPa pore pressure; see Fig. 9). This took approximately 2 days. The confining pressure was then decreased stepwise, until the axial strain started to accelerate. This procedure was chosen as an attempt to follow the failure envelope without exceeding it. After this, the sample was kept at constant confining pressure, increasing axial strain at a constant rate. The axial stress dropped, the sample dilated, and the test was terminated after 10 days.

S Shale was loaded to an initial state with axial stress = 37.6 MPa, confining pressure = 37.0 MPa and pore pressure = 17.9 MPa (see Fig. 10), representative of in situ conditions. The initialization took 3–4 days. The confining pressure was then reduced stepwise to 26 MPa, when failure initiation was detected by applying a pre-set strain rate threshold. After this, the axial stress was kept constant and the radial strain was kept zero in an attempt to follow the failure envelope. This seemed to move the sample away from failure, so the test was continued by manual switching to confining pressure control, keeping zero axial strain in the last part. The test lasted 21 days.

The pre-test examination of the shale samples shows no sign of fractures, see Fig. 11. The samples are relative homogeneous with visible horizontal layering. Post-test examination show evidence of shear failure in both samples. Note that the damage to the surface of the S Shale is most likely caused by pressure release during final unloading (post-test). The Pierre Shale have more fractures than the S Shale and shows clear evidence, in form of damage area around the open fracture, that large deformation is caused by slip along fracture planes. Examination of S-Shale after testing shows large deformation along one shear plane (Fig. 11, middle right), however, no significant damage was seen in the area around the fracture.

5.2. Experimental results from borehole stress path tests

The primary purpose of the borehole stress path tests described in the previous section was to see how ultrasonic velocities change when shales are brought to failure along a stress path relevant for conditions near an open hole or near the wall of an annulus outside a casing. Fig. 9 shows stresses and strains versus time for the test performed in the laboratory with Pierre I Shale in order to simulate the impact of near well stresses on mechanical behaviour. The first steps prior to reaching the initial stress state are included for completeness, showing that the sample compacted volumetrically by ~25 milliStrain in this part of the experiment. During subsequent radial unloading, strains were small until the radial stress reached 7 MPa. At that level, the sample started to dilate. A distinct planar shear failure was generated when the confining pressure dropped to 6 MPa. The axial stress could no longer be maintained at 20 MPa and dropped to about 10 MPa. The pore pressure was 4.9 MPa (in drained conditions).

In S Shale (Fig. 10), the stresses, including the pore pressure, were higher than in the test with Pierre I Shale. The initial net mean stress was 20.2 MPa for S Shale, compared to 10.3 MPa for Pierre I Shale. The sample compacted by ~30 milliStrain during loading to the in situ stress state. Volumetric expansion was small during radial and subsequent axial and radial unloading, until the radial (and hence volumetric) strain accelerated after reaching 31 MPa axial stress and 21.5 MPa confining pressure. Further lowering of both axial and radial stress maintained the state of failure and eventually led to further volumetric expansion. Fig. 12 shows the q-p' plots for both shales, where the peak stresses from the triaxial and the creep tests above are included as separate data points. In agreement with the strain data, the stress paths for both shales converge towards failure during initial unloading, remaining close to failure during final unloading. Failure initiation in Pierre I Shale was noticed at $p' \approx 5.8$ MPa and $q \approx 14.1$ MPa. From Fig. 12 S Shale appears to have been close to the failure surface at $p' \approx 12.2$ MPa and $q \approx 12.5$ MPa, but with no associated change in recorded strain rates. Measured strains suggest a subsequent failure onset at $p' \approx 6.9$ MPa and $q \approx 9.8$ MPa, and then again in the very end of the test ($p' \approx 1.0$ MPa and $q \approx 1.7$ MPa). The manual control of the experiment did not permit to maintain failure state throughout the test but has contributed to characterizing the entire failure surface and in particular the change of wave velocities along it.

Fig. 13 shows ultrasonic velocities against net mean stress for both shales, and velocities at selected p',q - levels are listed in Table 4. Like in the triaxial tests and the creep tests shown above, the velocities in Pierre I Shale are higher than the corresponding velocities in S Shale. The P-

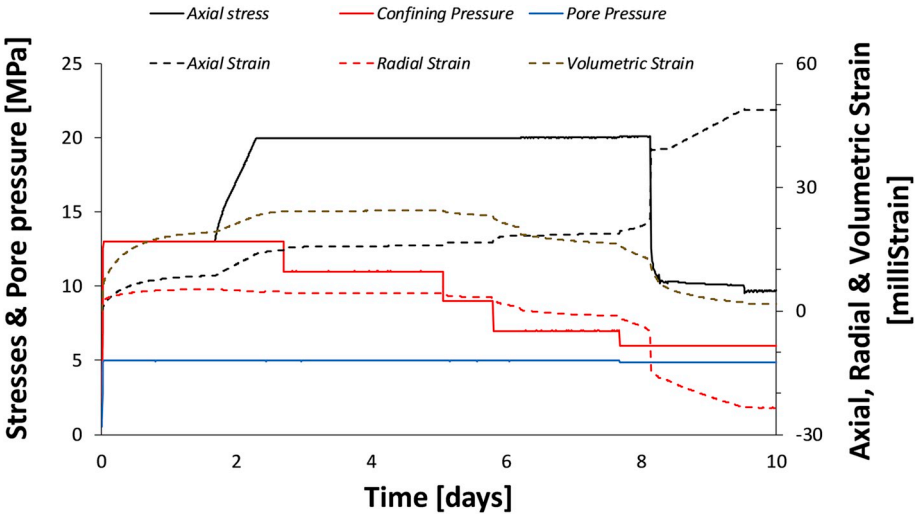

Fig. 9. Timeline for stresses, pore pressure and strains during the simulated borehole failure experiment with Pierre I Shale.

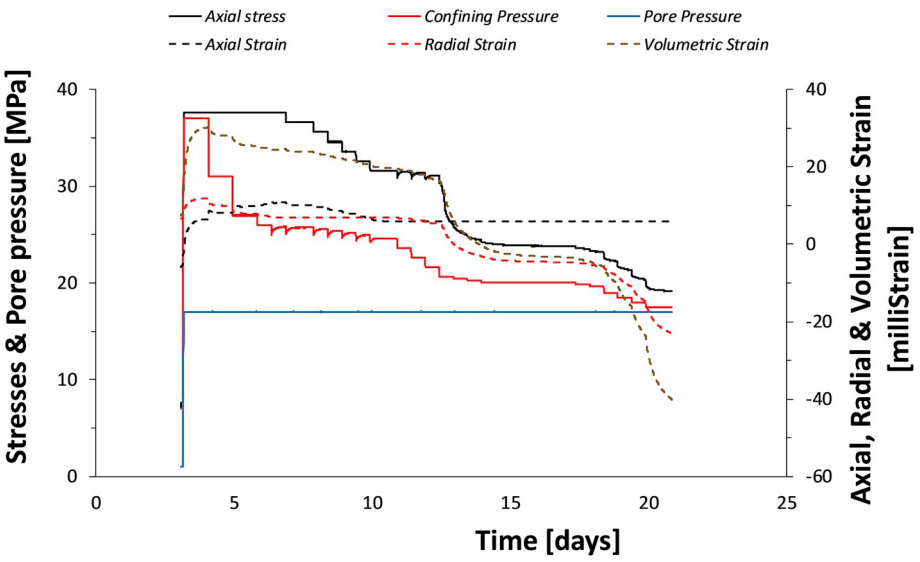

Fig. 10. Timeline for stresses, pore pressure and strains during the simulated borehole failure experiment with S Shale.

wave velocity normal to bedding at start of the radial unloading (10.3 MPa net stress) in Pierre I Shale was ~2835 m/s, while in S Shale (at 20.2 MPa) it was ~2127 m/s. Notice the initial P-wave anisotropy, with radial P-wave velocity of 2705 m/s in S Shale (exhibiting close to transverse isotropy; therefore only one radial mode is included in the Figure; P-wave anisotropy expressed by Thomsen's ε was 0.31). P-wave velocities were 3065 and 3120 m/s in two orthogonal radial directions in Pierre I Shale (hence in slight violation of the commonly observed transverse isotropy; with P-wave anisotropies ~ 0.08–0.10). Notice that all measured velocities during the test are displayed in the figure, including measurements during pore pressure equilibration periods. Since the velocity changes during each step are relatively small, this has little impact on the observed trends.

All velocities decreased with decreasing mean stress. Before failure initiation was approached, the axial P-wave velocities changed very slowly in both shales. The radial velocities decreased significantly faster, as a result of the primarily radial stress reduction. The decrease is much stronger in Pierre I Shale (near 50 m/s MPa^{-1} for both radial P-waves) than in S Shale (just below 10 m/s MPa^{-1}). After failure initiation all velocities dropped dramatically in Pierre Shale, while they continued to decrease at a similar rate as prior to failure in S Shale. As a result, there was no velocity anisotropy in Pierre I Shale at the end of the test, with all P-wave velocities around 2500 m/s. In S Shale, the P-wave anisotropy was maintained: Thomsen's ε was 0.31 also at the end of the test. As mentioned before, *R*-factors are strongly stress path dependent (Holt et al., 2018), and since the stress path varied throughout these tests, it does not make sense to compute their values.

The spectral attenuations of the P-wave signals for Pierre I and S Shale, measured at 500 kHz, are shown in Fig. 14. In both cases there is an increase in attenuation during failure with decreasing mean net stress. This effect is particularly large in Pierre I Shale, and it is in both cases much larger for the axial than for radial P-waves.

As seen above (Fig. 12) these tests largely confirm the failure envelope developed by the undrained triaxial and constant mean stress (creep) tests described before. They contribute to estimation of the (q, p')-failure surface, in particular for low mean net stress, which may be representative for a shale barrier in the forming, or for a borehole close to collapse. In particular, the relationship between P-wave velocities and net mean stress seems to be much less affected by the failure process in ductile S Shale than in brittle Pierre Shale, also in agreement with the triaxial and the creep tests above. This has possible implications for logging of shale barriers, that will be described in the Discussion below.

6. Discussion

6.1. Possible field implications of mechanical behaviour

Both rocks studied in this work are soft, low strength shales, typical of relatively young overburden formations in offshore basins. The experimental studies presented above show that small differences in mechanical properties can lead to significant differences in mechanical behaviour controlling borehole failure: Pierre I Shale fails in a predominantly brittle ("sloughing") manner, while S Shale exhibits a more ductile ("gumbo" like) behaviour, although it also fails with strain localization. Both shales might cause drilling problems (tight hole/stuck pipe) in a field situation, depending on factors that are partly given by nature (in situ stresses and pore pressure) and partly by the drilling strategy (mud weight, mud composition, drill angle and azimuth with respect to the stress field). Further analysis of the impact of plasticity/brittleness on borehole collapse is given by Holt et al. (2015).

Most likely Pierre I Shale would not easily form a barrier around a casing, because of its brittle behaviour. This was confirmed by independent shale barrier tests in the laboratory (Fig. 1, left). S Shale is known to make a barrier, both from laboratory tests (Fig. 1, right) and field observations. The plastic yielding mode is favourable for the formation of shale barriers. This behaviour can be assessed from the q-p' plots made on basis of triaxial tests (Fig. 2, and to some extent Fig. 6 from the CU creep test): These demonstrate that S Shale behaves more like a normally consolidated clay, whereas Pierre I Shale exhibits behaviour characteristic for an overconsolidated or slightly cemented shale. Considering the characterization data shown in Table 1, further differences between the two shales are mainly the significantly higher porosity and the lower friction angle of S Shale. S Shale also has lower unconfined strength and slightly higher clay content than Pierre I Shale. In addition to stress and stress history, all these parameters influence the difference in willingness to create shale barriers.

6.2. Microscopic interpretation of ultrasonic measurements

The differences in wave velocity behaviour between the two shales is pronounced: Not only does Pierre I Shale show higher velocities (Tables 2–4), characteristic of a stiffer and less porous material, but the stress dependence both prior to and after failure initiation (Figs. 3, 7 and 13) is significantly larger than for S Shale. In addition, the ultrasonic attenuation associated with the failure process is much larger in Pierre I Shale than in S Shale. These observations support the evolution of cracks

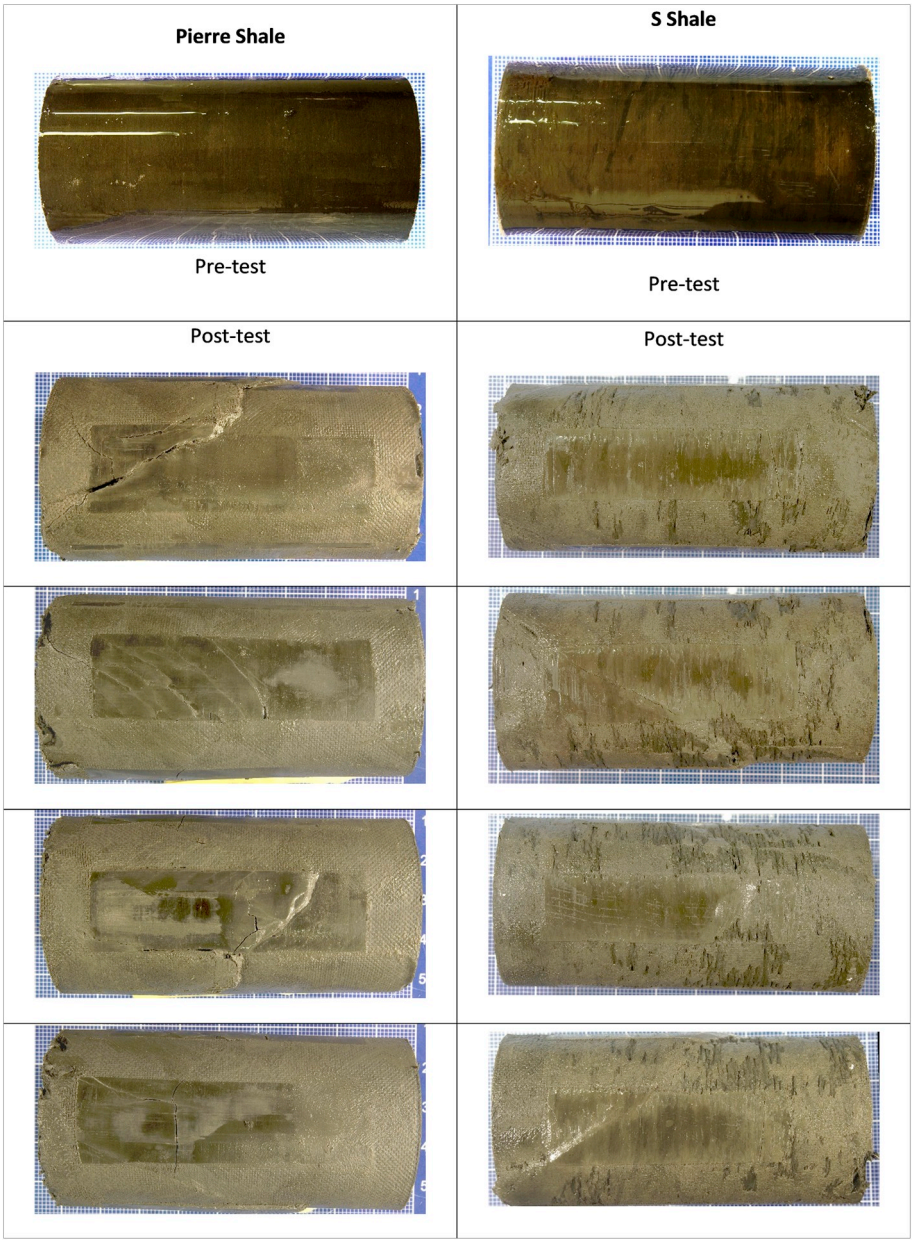

Fig. 11. Pictures of shale cores before and after the simulated borehole stress tests. The left column shows Pierre Shale, and the right column shows S Shale. The pictures on the top of each column are taken before the tests, when the cores are wrapped in the plastic sleeve to avoid any dehydration. The lower 4 pictures in each column are different views of the rotated samples after the tests. The rectangular marks on the surfaces represent absence of permeable mesh for drainage to permit radial P-wave measurements. Depositional features such as burrows, not to be interpreted as core damage or fractures, are seen in S Shale prior to as well as post-test.

in both shales, and the observed stress dependent velocity and attenuation anisotropies indicate that cracks are opening primarily normal to the direction of maximum principal stress; i.e. radially.

The different orders of magnitude of stress sensitivity between Pierre I and S Shale must be related to the nature of the cracks. From several experiments with different rocks, macroscopic failure is seen to be preceded by opening of microcracks normal to the maximum principal stress, followed by coalescence and shear localization at an angle to the principal stress controlled by internal friction (Horii and Nemat-Nasser, 1985; Fjær et al., 1989). In our case, the formation of visible shear bands is more apparent in Pierre I Shale, in agreement with the ultrasonic observations. However, the changes in velocities prior to failure, which relate to closure of pre-existing cracks or soft pores primarily aligned with the bedding plane (here a plane of radial extent), are also much larger in Pierre Shale than in S Shale. These differences could be related to difference in saturation: It is commonly observed in sandstones and other lithologies that stress sensitivity is strongly reduced when a dry sample is saturated with liquid. We have reasons to believe that our shales are fully water-saturated, since they do produce expected undrained pore pressure response in the undrained experiments. The larger impact of cracks could then be due to crack drainage during dilation in Pierre I Shale, and opening of new cracks that become only partially saturated. An equally plausible explanation could be that a dominant part of the cracks in S Shale are smaller or located in narrower (nanometer scale) pores than in Pierre I Shale, so that water inside them transform to bound water with shear rigidity (Israelachvili and Wennerström, 1996; Antognozzi et al., 2001; Holt and Kolstø, 2017). This will reduce the elastic contrast between the cracks and their surroundings and hence make the cracks almost transparent to ultrasound. Such "nano-cracks" (Holt et al., 2017) could also be linked to creep and plastic deformation, controlled by the altered viscosity of the first molecular water layers near solid surfaces.

6.3. Impact on sonic and ultrasonic log responses

Sonic log data can be used to measure P- and S-wave velocities in target formations prior to completion. Such data are valuable for drilling of future wells in the same area and can be used to assess borehole

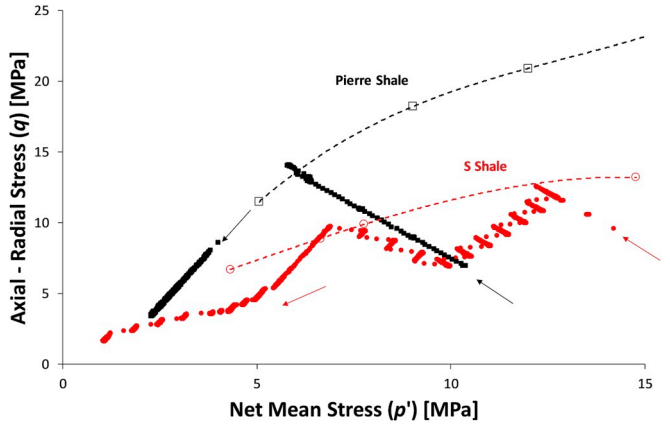

Fig. 12. *q–p'* plot for Pierre I Shale and S Shale for the tests performed along simulated borehole stress path tests. The additional (open) data points are from the separate consolidated undrained triaxial tests with the two shales, demonstrating that the borehole stress simulations managed to navigate close to the failure state.

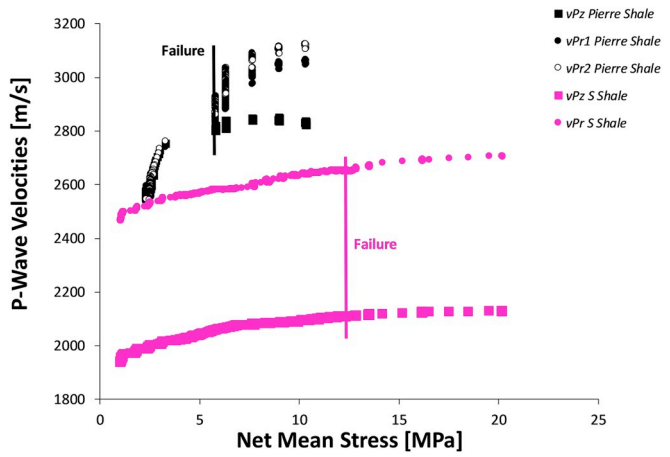

Fig. 13. Axial and radial P-wave velocities for Pierre I Shale and S Shale vs. net mean stress (= *p'*) from the borehole stress simulation tests (Figs. 9 and 10). The plot includes all measurement points, also during pore pressure equilibration periods. Radial velocities in the lab correspond to horizontal velocities in a field situation with a shale having vertical symmetry axis, and would be representative of ultrasonic pulse echo measurements, whereas axial velocities would be seen in open hole logs. The vertical black and pink lines represent failure identifications for Pierre and S Shale, resepctively. (For interpretation of the references to colour in this figure legend, the reader is referred to the Web version of this article.)

stability through correlations with mechanical properties like shale strength and static stiffnesses (e.g. Horsrud, 2001). For a vertical borehole through a horizontally bedded shale the acquired velocity would be that of the vertical P-wave, corresponding to v_{Pz} in the laboratory. Log derived P-wave velocities are however in the kHz range, which implies that correlations based on ultrasonic calibrations may not be directly used due to dispersion (e.g. Suarez-Rivera et al., 2001; Duranti et al., 2005). This is to some extent a matter of calibrating to field experience.

Ultrasonic velocities in most rocks tend to follow a decreasing trend with increasing porosity, alternatively with increasing density. The experimental data with Pierre I and S Shale are compared with previously seen trends for shales in Fig. 15. In this plot, acoustic impedances are compared with those of North Sea field shale cores from previous triaxial tests (see also Holt et al., 2017), and also with oil well cements (Allouche et al., 2006) The old lab data were obtained at a low effective confining press of 2 MPa, and the figure shows both data in the initial

Table 4
Axial and radial P-wave velocities after the initial state and at selected stress states (including failure initiation and beyond) in borehole stress simulation tests with Pierre I Shale and S Shale. Pr1 and Pr2 refer to two orthogonal radial directions that were monitored in the test with Pierre Shale.

Pierre I Shale	Stress state [MPa]	v_{Pz} [m/s]	v_{Pr1} [m/s]	v_{Pr2} [m/s]
	$p' = 8.0, q = 0$	2724	3015	3075
	$p' = 10.3, q = 0$	2835	3065	3125
	$p' = 5.8, q = 14.1$ (failure)	2805	2819	2872
	$p' = 2.5, q = 4.1$ (failure)	2562	2578	2542
S Shale	**Stress state [MPa]**	**v_{Pz} [m/s]**	**v_{Pr} [m/s]**	
	$p' = 20.2, q = 0.6$	2127	2705	
	$p' = 12.2, q = 12.5$ (failure ?)	2107	2648	
	$p' = 6.9, q = 9.8$ (failure)	2074	2585	
	$p' = 1.0, q = 1.7$ (failure)	1937	2465	

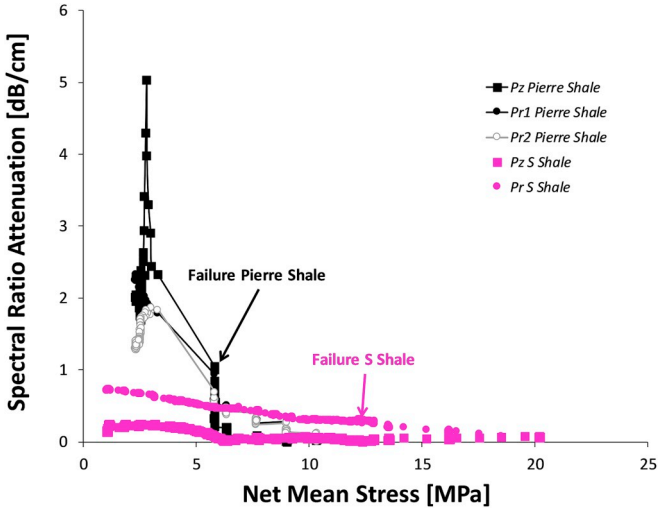

Fig. 14. Spectral attenuation vs net mean stress (*p'*) for axial and radial P-waves during the borehole stress simulation tests. The black and pink arrows represent failure identifications for Pierre and S Shale, resepctively. (For interpretation of the references to colour in this figure legend, the reader is referred to the Web version of this article.)

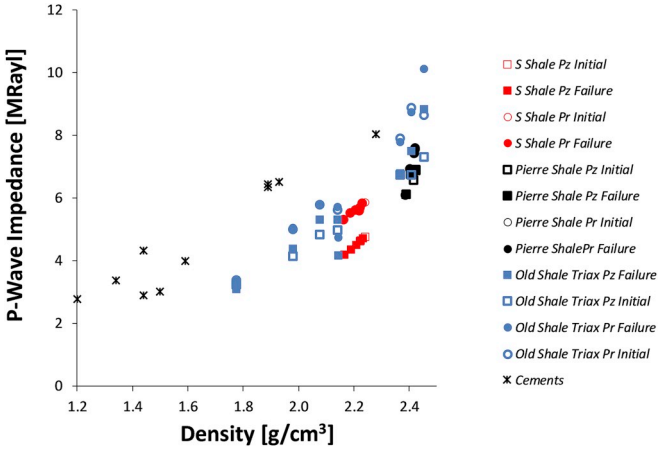

Fig. 15. Axial and radial P-wave impedance vs density for Pierre I Shale and S Shale in initial state and during failure in the borehole stress simulation tests (see Fig. 13). The figure also includes data from a set of previously tested shales, measured at failure in triaxial tests performed with 2.5 MPa confining pressure (Holt et al., 2017). Notice that 1 MRayl = 106 kg m^{-2} s^{-2}.

state and in the failure state during subsequent triaxial testing. From the present study, the data shown are from the borehole stress simulation experiments, both during initial loading and after failure was reached. The impedances are given by the measured velocities, and the density changes during the tests are estimated from the measured volumetric strains. Both Pierre I Shale and S Shale have axial and radial P-wave impedances that are slightly lower than those given by the trends of the old data, but they do show similar variations with shale density, and hence porosity. Note that for these shales as well as for the old data, there is insignificant difference between the impedances measured in the initial part of the tests and during failure. The barrier forming S Shale has axial P-wave impedance between 4 and 5 MRayl [1 MRayl = 10^6 kg m^{-2} s^{-1}], and the radial P-wave impedance is between 5 and 6 MRayl. The corresponding values for Pierre I Shale are between 6 and 8 MRayl, for both impedances. It appears that the acoustic impedance vs density cross-plot may give a guideline for identification of shales that may form a barrier, and that initial sonic log as well as density data may be used as a good indication. For pulse-echo probing of a cased vertical well through a horizontally bedded shale, the measured response would depend on the horizontal P-wave impedance. Translating to the laboratory experiments, this means the radial impedance = ρv_{Pr}. With the pitch-catch technique, which can be used as a supplement to the pulse-echo method, the attenuation of a flexural wave travelling along the casing is measured and related to the P-wave velocity of the contacting medium (cement, shale, etc). No analysis has yet been made of the impact of shale anisotropy on the measured flexural wave response.

Fig. 15 also includes impedances of typical cements (taken from Allouche et al. (2006)). For detection of a barrier behind the casing, it may be difficult to distinguish between cement and shale based on impedance alone. However, light-weight cements have much lower density and also higher velocities than shales, so if there is a separate measurement of one of these parameters from logs before completion or from pitch-catch data, they may be distinguished.

Velocities depend on the initial stress state, which in the field corresponds to the in situ stress state modified by the stress alteration in the near-well region. Most often sonic log data are thought to be representative for the virgin formation, anticipating that the penetration depths of the waves exceed the altered region. From the laboratory experiments, the differences between these velocities for S Shale seem to be small: If the net mean stress in the logging situation (controlled by the well pressure) is not dramatically different from the original net mean stress, the difference is 10–20 m/s for the axial P-wave velocity, and somewhat larger for the radial P-wave.

The effect of failure is also relatively small in S Shale. In both shales, velocities decrease after failure when the mean stress decreases, as can be seen from the borehole stress simulation test (Table 4 and Fig. 13). Given the relationship between p' and q defined by the failure criterion, it may be anticipated that velocities can be expressed as a unique function of p', in particular if the post-failure behaviour is characterized by plastic deformation rather than brittle fracturing. The velocities after failure initiation in Fig. 13 can be fitted to a power law of the form $v = a(p')^m$ both for Pierre I Shale and S Shale. The exponent m is ≈ 0.03 for both P-wave velocities in S Shale, including all measured velocities after failure initiation. The value for Pierre I Shale is higher ($\approx$0.08) but must be strongly influenced by localization. However, these observations mean that the velocity of a shale barrier will increase with increasing load on the casing, and hence may provide a dynamic indicator of barrier formation if monitored by a sufficiently accurate logging technique. It remains to be seen if the combined use of pitch-catch and pulse-echo tools can provide a feasible technique for monitoring of shale barrier evolution and if the sealing ability of the barrier may be quantified. Note that if load on casing may be estimated from log measurements, it might also constitute a valuable tool for estimating the probability of casing collapse.

Ultrasonic data similar to log response in the field can be acquired during hollow or cased cylindrical core tests in the laboratory. Such a set-up, including a miniature logging tool, has been developed in our laboratory (for a pre-study, see Sirevaag et al., 2018). The set-up provides data that can be processed and compared directly with raw log data from open hole or cement bond logs. In particular, the results presented in this paper may be of help to identify the transition from initial contact to formation of a sealing barrier.

7. Conclusions

The role of brittleness versus ductility plays an important role in borehole stability during drilling as well as in the formation of natural shale barriers around cased holes. Through different rock mechanical tests with two soft shales, brittle failure was observed in an outcrop (Pierre I Shale), and ductile failure was found in an overburden field material (S Shale). The difference between the two shales was most clearly illustrated by plotting shear stress against normal mean stress (so-called q,p' plots in soil mechanics terminology), where the trends for the two shales are opposite after failure initiation. This points to the stress history and possibly associated diagenesis (cementation) as a key in determining the post-failure behaviour. Other possible attributes that could be evaluated from core data are unconfined strength and friction angle, which both have lower values in the ductile than in the brittle shale. Normally core samples would not be available in a field situation, while log data might be – from the actual well in case of evaluating feasibility for barrier formation, and from neighbouring wells in the case of borehole stability prediction. In this case, high porosity (low density), high clay content and low sonic velocity can be used as indicators of ductility. Even seismic data might be utilized as a first indicator if velocities or reflection coefficients (incorporating acoustic impedance) can be determined.

Ultrasonic velocities were measured in all experiments, partly as a tool to understand the micromechanics of the failure process, and partly to improve the interpretation of open hole sonic and cased hole ultrasonic log data. In one of the experiments, failure was initiated along a stress path that mimicked stress change near a borehole or an annulus outside the casing. The more brittle Pierre I Shale showed larger stress sensitivity both prior to and in particular after failure initiation, which can be explained by evolution of damage in forms of microcracks and macroscopic failure planes. For the ductile S Shale, the velocity changes were much smaller, and the difference between intact and failed shale was minor. Even anisotropy, which was characteristic for both shales, was preserved during failure in S Shale. Ultrasonic attenuation measurements showed large increase in attenuation prior to and during failure in Pierre I Shale, and significant but less increase in S Shale. These observations indicate that less additional damage is necessary in order to fail the ductile S Shale, since the material is softer and thus has less cement and thereby less potential for new cracks, and further that the damage may occur in the form of smaller cracks on the nanometer scale which are fully or partly saturated with bound water. A practical consequence is that sonic log data in the intact formation may be used to assess the impedance of a possible naturally formed shale barrier outside the casing. An impedance – density crossplot provides a practical tool to distinguish barrier forming or “gumbo” (ductile) shale from less obvious barrier forming or “sloughing” (brittle) shale.

Author contribution statement

Rune M Holt Formal analysis, Methodology, Investigation, Data analysis, Writing original draft and review.

Idar Larsen Methodology, Software, Visualization, Data acquisition and analysis, contributing to writing and review, Project administration.

Erling Fjær Methodology, Formal analysis, Data acquisition and analysis, contributing to writing and review, Project administration.

Jørn F Stenebråten Data acquisition and analysis, contributing to writing and review.

Acknowledgements

The authors would like to acknowledge the sponsors of the KPN project "Shale Barrier Toolbox: Designing future wells for efficient completion and simpler P&A" (Grant no. 280650/E30) at SINTEF Industry. This project is sponsored by the Research Council of Norway, Aker BP ASA, BP Exploration Operating Company Ltd, ConocoPhillips Skandinavia AS, Equinor Energy AS, Lundin Norway AS, Petrobras and Total E&P Norge AS. We also acknowledge sponsorship from the past KPN project "Logging Shale Barrier before Well Abandonment" (Grant no. 255365/E30) at SINTEF Industry by the Research Council of Norway, Aker BP ASA, BP Exploration Operating Company Ltd., ConocoPhillips Skandinavia AS, Equinor Energy AS, Shell Exploration & Production Company and Total E&P Norge AS. Partial support was also granted through the PETROMAKS2 KPN-project: "Shale as a Permanent Barrier after Well Abandonment" at SINTEF Industry (Grant no. 244420), with the same sponsors.

Appendix A. Supplementary data

Supplementary data to this article can be found online at https://doi.org/10.1016/j.petrol.2019.106746.

References

Allouche, M., Guillot, D., Hayman, A.J., Butsch, R.J., Morris, C.W., 2006. Cement job evaluation. In: Nelson, E.B., Guillot, D. (Eds.), Well Cementing, second ed., vol. 15, pp. 549–612 Schlumberger, Ch.

Antognozzi, M., Humphris, A.D.L., Miles, M.J., 2001. Observation of molecular layering in a confined water film and study of the layer's viscoelastic properties. Appl. Phys. Lett. 78, 300–302.

Atkinson, J.H., Bransby, P.L., 1978. The Mechanics of Soils – an Introduction to Critical State Soil Mechanics. McGraw-Hill, p. 375.

DeBruijn, G., Elhancha, A., Khalilova, P., Shaposhinkov, P., Tovar, G., Sheperd, P., 2016. An integrated approach to cement evaluation. Oilfield Rev. 28, 10–19.

Duranti, L., Ewy, R., Hofmann, R., 2005. Dispersive and attenuative nature of shales: multiscale and multifrequency observations. In: 75th SEG Meeting. Expanded Abstracts, Houston, USA, p. 4.

Fjær, E., Holt, R.M., Raaen, A.M., 1989. Rock mechanics and rock acoustics. In: Maury, V., Fourmaintraux, D. (Eds.), Rock at Great Depth, pp. 355–362. Balkema.

Fjær, E., Holt, R.M., Horsrud, P., Raaen, A.M., Risnes, R., 2008. Petroleum Related Rock Mechanics. Elsevier, p. 491.

Fjær, E., Stenebråten, J.F., Bakheim, S., 2018. Laboratory test for studies on shale barrier formation. ARMA 7, 18-1146.

Gabrielsen, G.K., Stenebråten, J.F., Nes, O.-M., Holt, R.M., Horsrud, P., 2010. Use of Modified Hollow Cylinder Test in Laboratory for Simulation of Downhole Condition in Shale, SPE131356, p. 14.

Guenot, A., 1989. Borehole breakouts and stress fields. Int. J. Rock Mech. Min. Sci. Geomech. Abstr. 26, 185–195.

Hatchell, P., Bourne, S., 2005. Rocks under strain: strain-induced time-lapse time shifts are observed for depleting reservoirs. Lead. Edge 24, 1222–1225. https://doi.org/10.1190/1.2149624.

Havira, R.M., 1982. Ultrasonic cement bond evaluation. In: SPWLA 23rd Annual Logging Symposium, p. 11.

Hayman, A.J., Hutin, R., Wright, P.V., 1991. High-resolution cementation and corrosion imaging by ultrasound. In: SPWLA 32nd Annual Logging Symposium, p. 25.

Holt, R.M., Fjær, E., Stenebråten, J.F., Nes, O.-M., 2015. Brittleness of shales: relevance to borehole collapse and hydraulic fracturing. J. Petr. Sci. Eng. 131, 200–209. https://doi.org/10.1016/j.petrol.2015.04.006.

Holt, R.M., Fjær, E., Larsen, I., 2017. Ultrasonic properties of creepy shales. ARMA 6, 17-688.

Holt, R.M., Kolstø, M.I., 2017. How does water near clay mineral surfaces influence the rock physics of shales? Geophys. Prospect. 65, 1615–1629.

Holt, R.M., Bauer, A., Bakk, A., 2018. Stress path dependent velocities in shales: impact on 4D seismic interpretation. Geophysics 83, MR353–MR367. https://doi.org/10.1190/geo2017-0652.1.

Holt, R.M., Fjær, E., Larsen, I., Stenebråten, J.F., Raaen, A.M., 2019. On the border between brittle and ductile behavior of shale. ARMA 7, 19-2179.

Horii, H., Nemat-Nasser, S., 1985. Compression-induced microcrack growth in brittle solids: axial splitting and shear failure. J. Geophys. Res. 90 (B4), 3105–3125.

Horsrud, P., Sønstebø, E.F., Bøe, R., 1998. Mechanical and petrophysical properties of North Sea shales. Int. J. Rock Mech. Min. Sci. 35, 1009–1020.

Horsrud, P., 2001. Estimating mechanical properties of shale from empirical correlations. SPE Drill. Complet. 16, 68–73. https://doi.org/10.2118/56017-PA.

Israelachvili, J.N., Wennerström, H., 1996. Role of hydration and water structure in biological and colloidal interaction. Nature 379, 219–225.

Kristiansen, T.G., Dyngeland, T., Kinn, S., Flatebø, R., Aarseth, N.A., 2018. Activating Shale to Form Well Barriers: Theory and Field Examples. SPE-191607-MS, p. 23.

Van Kuijk, R., Zeroug, S., Froelich, B., Allouche, M., Bose, S., le Calvez, J.-L., Schoepf, V., Pagnin, A., 2005. A novel ultrasonic cased-hole imager for enhanced cement evaluation. In: International Petroleum Technology Conference, IPTC-10546-MS. https://doi.org/10.2523/IPTC-10546-MS.

Marsden, J.R., Dennis, J.W., Wu, B., 1996. Deformation and failure of thick-walled hollow cylinders of mudrock - a study of wellbore instability in weak rock. In: Barla, Balkema (Ed.), Proc. Eurock'96, pp. 759–766. Rotterdam.

Meier, T., Rybacki, E., Reinicke, A., Dresen, G., 2013. Influence of borehole diameter on the formation of borehole breakouts in black shale. Int. J. Rock Mech. Min. Sci. 62, 74–85.

Nes, O.-M., Sønstebø, E.F., Fjær, E., Holt, R.M., 2004. Use of small shale samples in borehole stability analysis. In: ARMA/NARMS 04-564, p. 11.

Røste, T., Stovas, A., Landrø, M., 2006. Estimation of layer thickness and velocity changes using 4D prestack seismic data. Geophysics 71, S219–S234. https://doi.org/10.1190/1.2335657.

Sirevaag, T.L., Johansen, T.F., Larsen, I., Holt, R.M., 2018. Laboratory setup for improved logging behind casing. In: SPWLA 59th Ann. Symp., p. 16.

Suarez-Rivera, R., Willson, S., Nakagawa, S., Nes, O.M., Liu, Z., 2001. Frequency scaling for evaluation of shale and mudstone properties from acoustic velocities. In: AGU 2001 Fall Meeting, San Francisco, December 10–14, Paper No. T32E-0924.

Williams, S., Carlsen, T., Constable, K., Guldahl, A., 2009. Identification and Qualification of Shale Annular Barriers Using Wireline Logs during Plug and Abandonment Operations. SPE/IADC 119321.